

STEM electron beam-induced current measurements of organic-inorganic perovskite solar cells



M. Duchamp^{a,b,*}, H. Hu^a, Y.M. Lam^a, R.E. Dunin-Borkowski^b, C.B. Boothroyd^{a,b}

^a School of Materials Science and Engineering, Nanyang Technological University, 50 Nanyang Technological University, Singapore 639798, Singapore

^b Ernst Ruska-Centre for Microscopy and Spectroscopy with Electrons (ER-C), Forschungszentrum Jülich, Jülich, 52425, Germany

ABSTRACT

We describe a new approach for preparing organic-inorganic perovskite solar cells for electron beam-induced current (EBIC) measurements in plan-view geometry. This method substantially reduces sample preparation artefacts, provides good electrical contact and keeps the preparation steps as close as possible to those for real devices. Our EBIC images were acquired simultaneously with annular dark-field scanning transmission electron microscopy images using a home-made highly sensitive EBIC amplifier. High-angle annular dark-field images and energy dispersive X-ray maps were recorded from the same area immediately afterwards. This allowed the EBIC contrast to be correlated with regions containing N and a deficiency of O. The EBIC contrast was also found to be similar to secondary electron contrast recorded with a scanning electron microscope. By identifying the generation and absorption electron processes, we determine that EBIC cannot be separated from the secondary electron and absorbed currents. This means that careful analysis needs to be performed before conclusions can be made on the origin of the current measured across *p-n* or *p-i-n* junctions.

1. Introduction

Electron beam-induced current (EBIC) is a technique where the charge carriers generated by scanning an electron beam across an electrically contacted semiconductor device are collected and measured. The presence of local defects or internal fields affects the recombination and collection process, thus the current collected at the location of the electron beam differs compared to the bulk of the device. This technique was developed and widely used in the 1970's and early 1980's. At the time, it was mainly applied inside a scanning electron microscope (SEM) to locate *p-n* junctions or estimate the minority diffusion length. An extensive review of the understanding of EBIC and the experimental work at the time is given by Leamy [1]. More recently, EBIC experiments have been focused more on the study of solar cell devices rather than on devices for microelectronic applications due to the low dimensions of today's microelectronic devices which are not suitable for SEM observations.

The electronic properties of extended defects can only be fully understood if electrical measurements are made with high spatial resolution. The aim here is to correlate the recombination processes with the defect type ideally at the nanometre scale. The combination of EBIC-SEM with other experimental techniques allows correlation of the electrical properties at the local scale with the structural or luminescence properties. One approach is to perform EBIC-SEM experiments on

bulk samples and transmission electron microscope (TEM) observations on similar thin samples. However, this does not guarantee that both observations correspond to the same area and makes it difficult to extract direct correlations between the structure and the local electrical properties [2,3]. More recently, EBIC-SEM combined with TEM observations have allowed the location, density and nature of misfit dislocations in a GaAs/InGaAs quantum well *p-i-n* solar cell to be determined [4]. To obtain unambiguous and simultaneous correlations between electrically active regions and crystallographic defects at high resolution, the ideal approach would be to perform the EBIC directly inside a TEM. Despite the numerous EBIC-SEM results reported, experimental investigations using scanning (S-)TEM-EBIC are rare [5–9]. Among the pioneers, Fathy et al. located defects in avalanche photo detectors using the EBIC-STEM technique and showed the defects to be phosphorus rich using electron energy loss spectroscopy [5].

In the last few years, EBIC-SEM has been applied to new types of organic/inorganic solar cells. The recent developments of organic/inorganic lead halide-based perovskite solar cells are impressive but still the conduction and degradation mechanisms are not fully known at the local scale. Such solar cells were investigated using cross-sectional EBIC-SEM by Edri et al. [10]. Despite the spatial resolution of ~100 nm, they were able to prove the *p-i-n* operation mode and to determine that the carrier extraction efficiency is higher for electrons than for holes. Another recent study focused more on the investigation of degradation

* Corresponding author at: Laboratory for in situ and operando electron nanoscopy, School of Materials Science and Engineering, Nanyang Technological University, Nanyang Avenue 50, Singapore 639798, Singapore.

E-mail address: mduchamp@ntu.edu.sg (M. Duchamp).

<https://doi.org/10.1016/j.ultramic.2020.113047>

Received 17 April 2018; Received in revised form 27 March 2020; Accepted 5 June 2020

Available online 11 June 2020

0304-3991/ © 2020 Elsevier B.V. All rights reserved.

mechanisms at the nanometre scale by performing *in situ* TEM observations of such solar cells under electrical bias. This work led to the visualization of a number of degradation pathways. Among these are iodide migration at the positively biased MAPbI₃ interface and the volatilization of organic species triggering the nucleation of PbI₂ nanoparticles. These were found to be responsible for the decrease in cell performance [11].

After a general discussion of EBIC theory, we describe our experimental setup used to perform EBIC-STEM measurements on organic/inorganic lead halide-based perovskite solar cells. In Section 4, we present simultaneous ADF-STEM (annular dark-field) and EBIC-STEM combined with EDX-STEM (energy-dispersive X-ray spectroscopy) results obtained in plan-view geometry for a cell made directly on a dedicated MEMS-support. In Section 5, we present our understanding of the experimental results.

2. General considerations

2.1. EBIC theory in cross-sectional geometry

The aim of EBIC studies is often to be able to extract quantitative physical parameters namely the minority carrier diffusion length and lifetime and surface recombination velocities. EBIC can also be used as a qualitative technique to extract information such as the location of *p-n* junctions, spatial non-uniformity of the electrical properties or the location of recombination centres. Recombination centres can be caused by electrically active defects, dislocations and precipitates. A simplified understanding of EBIC, for *p-n* junctions or dislocations in the normal-cross-section geometry, i.e. with the *p-n* junction or dislocation interface parallel to the beam direction, is given by the well-known experimental relation that links the minority carrier diffusion length (*L*) and the EBIC (*I*_{EBIC}) [12]:

$$I_{EBIC}(x) = I_0 \exp(-x/L) \quad (1)$$

Here *I*₀ is the EBIC current at the interface and *x* the distance from the interface to the electron beam. This relation, unfortunately, holds only when the carrier recombination velocity (*V*_s) at the surface is non-zero, and better if the beam is far from the *p-n* junction or the dislocation interface. To overcome this limitation, a simple but improved formula has been established by Ong *et al.* based on the use of an empirical expression for the EBIC collected [13]:

$$I_{EBIC}(x) = k x^\alpha \exp(-x/L) \quad (2)$$

where α is related to the recombination velocity ($\alpha = 0$ for $V_s = 0$, and $\alpha = -1/2$ for $V_s = \infty$) and *k* is a constant. The authors demonstrate both the diffusion length and the recombination velocity can be extracted from experimental data using Eq. (2).

Beginning in the late 1970's, more complex analytical expressions for the recombination velocity at grain boundaries [14] and the minority carrier diffusion length and lifetime at *p-n* junctions or Schottky barriers [15–17] were established. Despite these models including surface recombination, they assume a Gaussian-type generation volume that makes them valid only outside the depletion regions. A later model for quantitative evaluation of the EBIC profile, introduced by Bonard and Ganière, uses a more realistic function describing the generation of electron-hole pairs and accounts for electron-hole pair generation inside the depletion region [18,19]. They applied this expression to *p-n* junctions in GaAs/Al_{0.4}Ga_{0.6}As heterostructures and obtained a diffusion length with a precision of $\pm 0.1 \mu\text{m}$, as well as values for the surface recombination velocity to diffusivity ($D=L^2/\tau$) ratio, τ being the minority carrier lifetime.

2.2. EBIC theory in planar geometry

In the previous section, in cross-section geometry, the EBIC was given as a function of the electron beam interface distance. In the

planar geometry case, this distance is in the electron beam direction and thus is not relevant. Nevertheless, planar geometry can be used to determine the location of *p-n* junctions and can be applied to field effect transistors in operation [1]. More interestingly, the presence of defects acting as recombination centres in a region having an internal field, like a *p-n* junction or the active part of a solar cell, reduces the EBIC locally. As for cross-sectional geometry, analytical expressions have been established to relate the EBIC contrast to the presence of local defects both for SEM and STEM experiments. In these models, the defects lying in the *p-n* layers are regarded as a perturbation of the theory discussed in the previous Section 2.1. According to this model, in the EBIC-SEM case, the contrast and resolution of the EBIC-SEM map are calculated as a function of the defect depth that can be probed by varying the acceleration voltage. The presence of a defect in the *n* layer at the top surface is shown to strongly modify the contrast of the EBIC-SEM images when most of the generation volume is inside the *n* layer (for lower acceleration voltages). In the same paper, Donolato also discussed the EBIC-STEM case and showed that the position of the defects within the *n* layer affects both the contrast and the resolution in a monotonic fashion [2,20].

2.3. Optimal sample geometry for EBIC-STEM

As previously mentioned, two geometries are available to perform EBIC studies, cross-sectional or plan view, depending on the information we want to extract. The cross-sectional geometry is better suited for the study of the lateral distribution of the internal field (Section 2.1.). However, the preparation of cross-section specimens for TEM observation is more delicate when electrical contacts have to be added to the TEM sample and may lead to surface artefacts [11,21]. On the other hand, the plan view geometry is more appropriate for detecting inhomogeneities of the electrical activity in *p-n* or *p-i-n* junctions and to relate them to structural or chemical defects. Fathy *et al.* reported one of the rare successful EBIC-STEM experiments based on this plan-view geometry [5]. Moreover, if fabricated on an electron transparent support, *in situ* TEM devices can be produced in a similar way to conventional devices, avoiding sample preparation artefacts.

In this paper, we report our study of organic/inorganic lead halide-based perovskite solar cells that are by nature thin enough to be electron transparent [20]. The aim is to locate the position of electrically active defects using EBIC-STEM and to determine the local composition at these defects. This can then be related to the failure mechanism of the solar cells. For this system, the plan-view geometry has the advantage of allowing the perovskite layer, which is air and humidity sensitive, to remain encapsulated between the electrical contacts and thus prevent degradation during the brief transfer from the controlled glove-box atmosphere to the TEM.

3. Materials and methods

The cell architecture investigated is described elsewhere [22]. The conventional layer stacking of our solution-processable solar cells consists of ITO/PEDOT:PSS/CH₃NH₃PbI₃/PC₆₁BM/Al layers on top of a glass substrate. The PEDOT:PSS and PC₆₁BM layers act as hole and electron transport layers (HTL and ETL), respectively.

We propose a new way of preparing a sample suitable for EBIC-STEM on dedicated MEMS-based chips that are designed to fit into a double-tilt "Lightning" DENSSolutions TEM holder. The electrical contacts from the holder to the chip are made using needles which access the specimen from the top. In order to have a working solar cell *in situ* in the TEM, both the top and bottom solar cell contacts need to be accessed independently by the needles. Our idea is to have the full solar cell deposited only in the middle of the MEMS chip, at the location of the electron transparent SiN window where the TEM observations are performed, while the top and bottom contacts are accessible on either side of the window (Fig. 1a and b). The low stress SiN window is

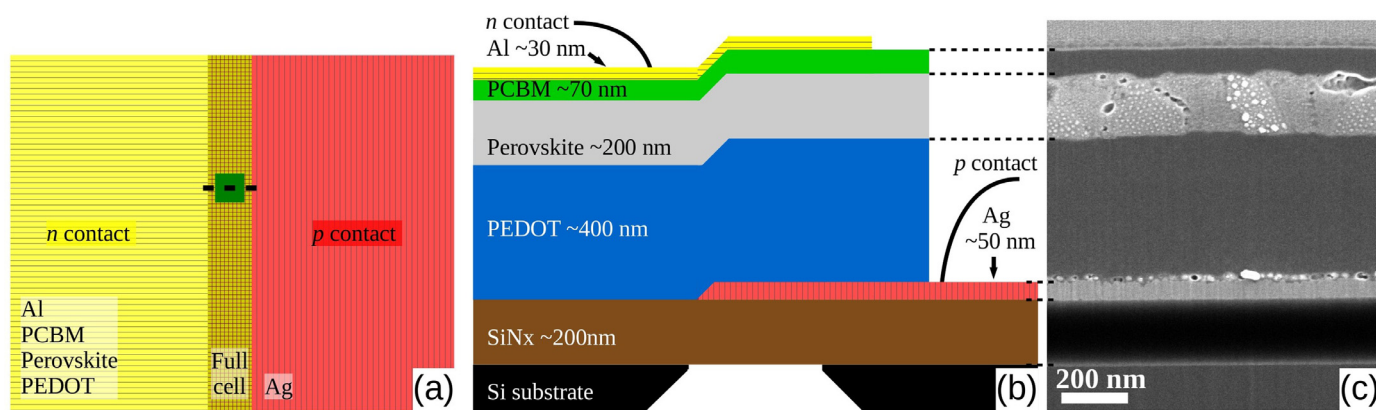


Fig. 1. (a) Diagram of the custom-made MEMS TEM support. The metallic layers (Ag and Al) were deposited by evaporation while the other layers were spin-coated. The Ag contact (red vertical hashing) was deposited first, the PEDOT:PSS, $\text{CH}_3\text{NH}_3\text{PbI}_3$ and PC_{61}BM layers were then spin-coated inside a glove-box. Finally, the top Al layer was evaporated (yellow horizontal hashing). The full cell structure is only present where the two metallic contacts overlap at the centre of the chip (orange square hashing). The green square in the middle of the overlap region indicates the location of the electron transparent SiN_x window where EM observations were performed. (b) Schematic cross-section of the solar cell layers deposited onto a custom-made MEMS TEM support. The region where all the layers overlap contains a full perovskite solar cell. (c) SEM cross-sectional image of an area adjacent to the electron transparent window, i.e. an area which contains all the layers. (For interpretation of the references to colour in this figure legend, the reader is referred to the web version of this article.)

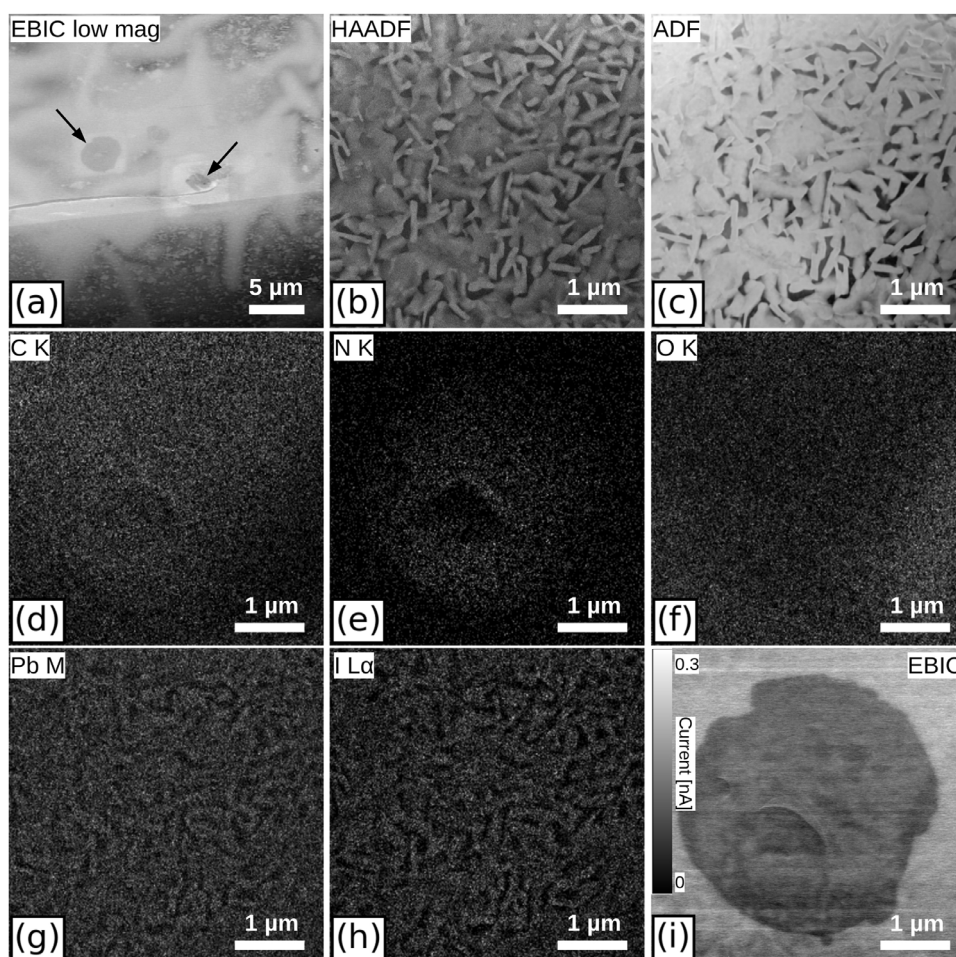


Fig. 2. (a) Low magnification EBIC-STEM map of the area studied at higher magnification in (b-i). (b) HAADF-STEM, (c) ADF-STEM, (d-h) EDX-STEM and (i) EBIC-STEM images recorded from the same area. EDX maps integrated from the (d) C K, (e) N K, (f) O K, (g) Pb M and (h) I L_{α} edges are shown. The HAADF-STEM image was recorded first, then the EBIC-STEM (i) and ADF-STEM (c) images were recorded simultaneously followed by the acquisition of the EDX-STEM data set from which the maps (d-h) were extracted. The intensity scale of the EBIC-STEM image is shown at the left of (i) in nA.

200 nm thick to prevent failure of the window during spin-coating of the layers.

The metallic layers (Ag and Al) were deposited by evaporation while the other layers were spin-coated. Ag was used instead of the ITO used in conventional solar cell structures for better electrical conductivity. The Ag contact (red with vertical shading, Fig. 1a and b) was deposited first and its area defined by a shadow mask. Then, the PEDOT:PSS/CH₃NH₃PbI₃/PC₆₁BM layers were spin-coated inside a N₂-filled glove-box. Finally, the top Al layer (yellow with horizontal shading, Fig. 1a and b) was deposited through a shadow mask on the opposite side to the Ag contact. The full cell structure is only present where the two metallic contacts overlap at the centre of the chip (orange with horizontal and vertical shading, Fig. 1a). In order to access the bottom Ag contact with the TEM holder needles, the solution-processable solar cell was dissolved down to the Ag layer where no Al was evaporated using a drop of acetone. In this way, the top Al and the bottom Ag contacts are accessible by the holder needles on the left and right sides of the chip respectively. A schematic diagram of the layer stacking sequence around the electron transparent SiN window is given in Fig. 1b and the corresponding cross-sectional SEM image shown in Fig. 1c. This innovative way to make connections to devices in a TEM without the use of FIB or other techniques that can introduce artefacts during the TEM sample preparation paves the way for easy *operando* experiments *in situ* in a TEM.

Secondary and backscattered electron imaging inside an SEM were performed using an FEI dual-beam FIB Helios workstation. Characterisation, including HAADF-STEM imaging, EDX-STEM and EBIC-STEM experiments, was performed using an FEI Titan probe-corrected TEM operated at 200 kV [23]. The EBIC-STEM and the simultaneously recorded ADF-STEM images were recorded with 1024 × 1024 pixels, a dwell time of 100 μs and a ~1 nA beam current.

The EBIC-STEM was measured using a custom-built amplifier with an amplifying factor of 2 V/nA whose output was connected to the analogue input of the Gatan DigiScan II control unit. The outputs of the sample were connected to two I/U converters (LMP7721 operational amplifier). The input impedance of the I/U converters was set to 10 MΩ, by the selection of their feedback resistors. The outputs of the I/U converters are fed to an instrumentation amplifier of the type INA163 with a gain of 100. The bandwidth is about 800 kHz, limited by the instrumentation amplifier.

In the rest of the manuscript, HAADF, ADF, EBIC and EDX refer to HAADF-STEM, ADF-STEM, EBIC-STEM and EDX-STEM unless otherwise stated.

4. Results

4.1. Simultaneous ADF/EBIC/EDX imaging

Fig. 2a shows a low magnification EBIC image taken at the edge of the SiN window. The dark contrast in the lower part of this image is due to the larger thickness of the MEMS chip outside the electron transparent window. Two areas, shown by black arrows in Fig. 2a, with a darker contrast near the middle are clearly visible. Normally for EBIC images, a lower intensity (and thus lower induced current) corresponds to an area with more recombination centres. Higher magnification images of the same area are shown in Fig. 2b–i. The HAADF image shown in Fig. 2b was recorded shortly before the simultaneously recorded EBIC (Fig. 2 i) and ADF (Fig. 2c) images. These were followed shortly after by the EDX data (Figs. 2d–h), all from exactly the same area. The small-scale contrast variations in the ADF (Fig. 2c) and HAADF (Fig. 2b) images match with the contrast variation recorded for the Pb and I EDX images (Fig. 2g and h). This is because the HAADF signal depends mostly on the heavy elements present. In contrast, the EBIC image shows a very different feature which is not related to the heavy elements but corresponds most closely to the N EDX map (Fig. 2e).

Fig. 3 shows two EDX spectra integrated inside and outside the dark feature in the EBIC image. By averaging over both the dark feature and the region outside it, the integrated spectra clearly show the presence of the different elements. More interestingly, the difference spectrum between the two areas enhances the composition variations. Within the area of dark EBIC contrast, there is more C and N while outside the O peak is stronger. No significant difference for the other elements is observed. The change in the O and C content is hardly visible from the EDX maps alone. The interpretation of the different amounts of C is difficult to attribute as C can build up due to contamination. Moreover EDX is not the method of choice to estimate C concentrations, so we will not speculate on the origin of the C signal. In contrast, N and O seem to have the same spatial variation as the EBIC signal.

4.2. Secondary electron imaging

Fig. 4 a–c are SE images recorded at different acceleration voltages: (a) 5 kV, (b) 2 kV and (c) 1 kV at the same location as Fig. 2. By changing the accelerating voltage we can probe different depths in the specimen, with higher voltages corresponding to images from deeper inside the specimen. At 5 kV, both the large EBIC dark features and contrast from the Pb and I in the perovskite layer are visible in the SE images. At lower voltages, i.e., 2 kV and 1 kV, the perovskite layer is not visible any more and only surface features can be seen. This indicates that Pb and I are located deeper inside the solar cell compared to the elements responsible for the dark EBIC features. Interestingly, smaller areas of dark contrast are visible at all three acceleration voltages (two such features are shown by red arrows in Fig. 4a–c), so they are also located on the topmost surface and probably have the same origin as the larger dark areas. We also observe bright rectangles that correspond to the areas scanned by the 200 kV STEM electron beam for the large amount of time needed to acquire the EBIC images. To confirm the composition of the dark EBIC spot, we also recorded a back-scattered electron (BSE) image inside the SEM at the same location (Fig. 4d). The intensity of back-scattered electron images depends mostly on the atomic number of the volume probed by the electron beam like for HAADF images. From this series of SEM images it is relatively clear that the EBIC contrast observed originates from or very near to the top surface of the solar cell.

5. Discussion

When a specimen is irradiated by a highly energetic electron beam, the interaction of the beam with the sample generates emitted electrons and currents as shown in Fig. 5a. Note that the arrows in Fig. 5 and the currents used in the equations represent the flow of electrons, not conventional current. For a thin specimen irradiated by high energy electrons (eg 200 kV) as in TEM and STEM, most of the incident electrons, I_0 , are transmitted either after elastic scattering (diffraction), inelastic scattering (where from a few to a few thousand eV are lost) or no scattering at all and form the transmitted beam, I_t . Thus the transmitted current, I_t , is approximately equal to but slightly less than I_0 with the remaining current, $I_{abs} = I_0 - I_t$, “absorbed” by the specimen.

In addition, secondary electrons (SE) and Auger electrons are generated and emitted from both the top and bottom surfaces. Most of this current, I_s , is due to SE and typically many low energy SE are generated for each primary electron (although with fewer secondary electrons as the beam voltage increases [24]), making $I_s > I_0$. The SE signal is very sensitive to the surface of the specimen. Recently, atomic resolution SE-STEM imaging has been demonstrated and shown to provide additional information compared to standard STEM techniques using conventional SE detectors. The SE-STEM imaging mode has been shown to be a perfect tool to image the surface of a sample, both at medium resolution [25] and at the atomic scale [26].

If the specimen is conducting and grounded (earthed), then a ground current (or specimen current), I_e , will flow to maintain

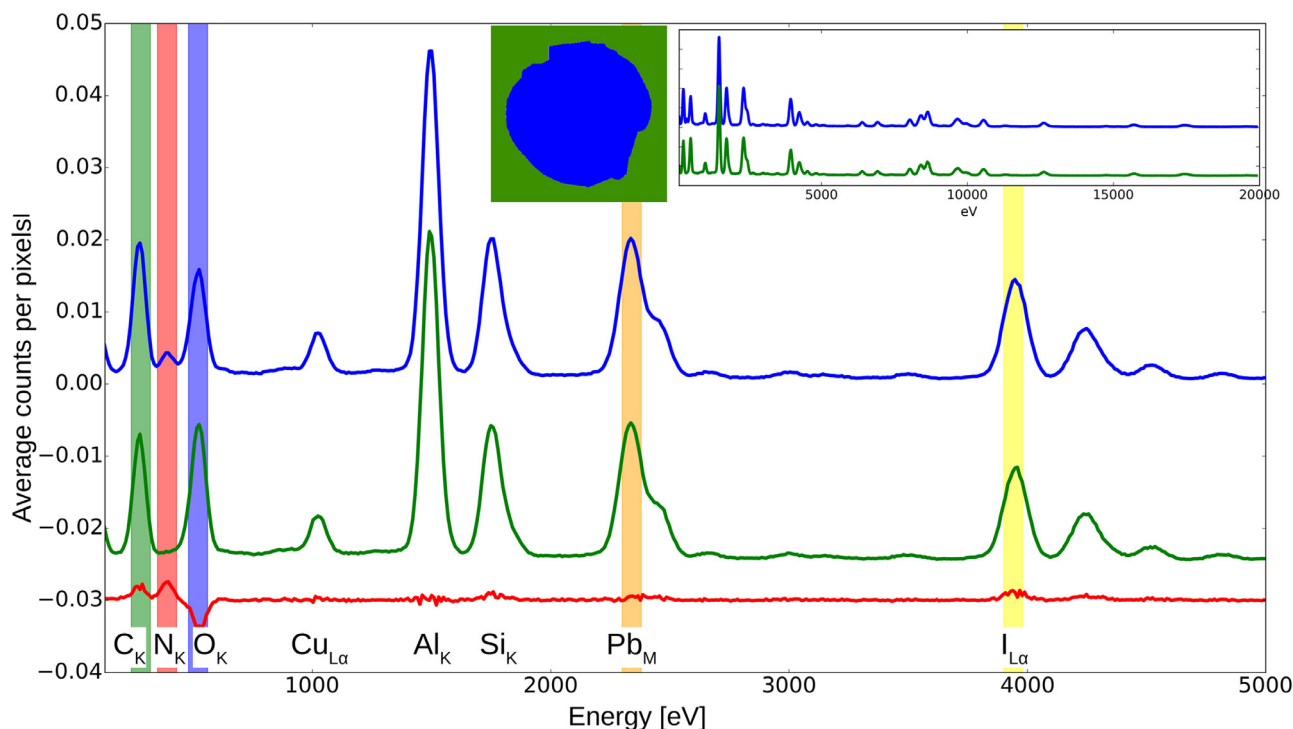


Fig. 3. EDX spectra averaged inside (blue) and outside (green) the areas (shown in the inset) corresponding to the high and low contrast regions of the EBIC-STEM map (Fig. 2i). The green spectrum is shifted vertically for clarity. The red spectrum is the difference between the average spectrum taken inside (blue) and outside (green) the dark area in Fig. 2i. The energy windows used for the EDX maps in Fig. 2d–h are shown as coloured regions labelled at the bottom. (For interpretation of the references to colour in this figure legend, the reader is referred to the web version of this article.)

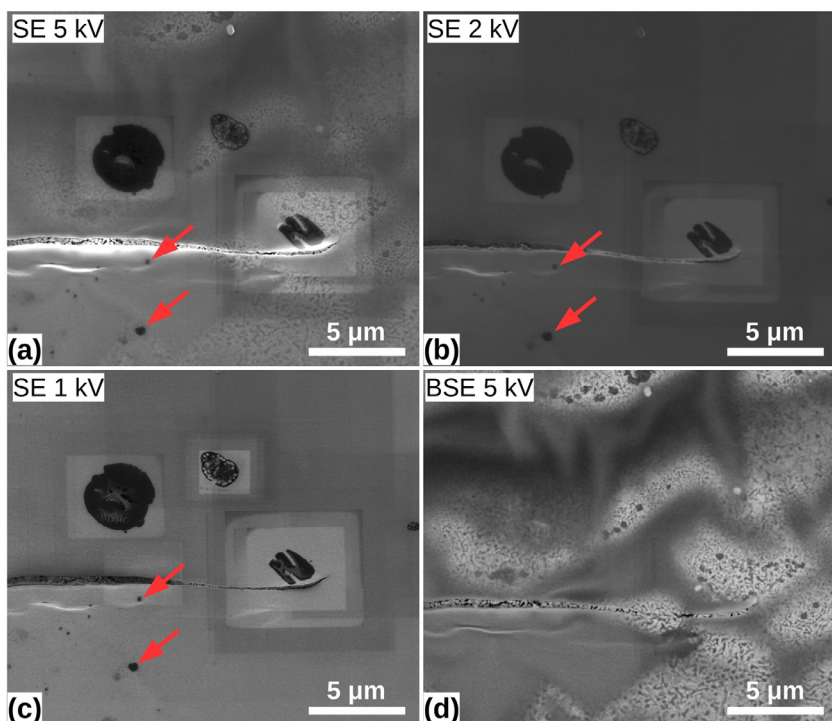


Fig. 4. (a–c) SEM secondary electron images of the area studied in Fig. 2 recorded for acceleration voltages of (a) 5 kV, (b) 2 kV and (c) 1 kV. (d) Backscattered electron image of the same area recorded at 5 kV. The red arrows in Figs. 4 a–c show the small dark contrast features located at the surface of the specimen referred to in the text. (For interpretation of the references to colour in this figure legend, the reader is referred to the web version of this article.)

neutrality where

$$I_0 + I_e = I_t + I_s$$

so that

$$I_e = I_s - I_{abs} \tag{3}$$

Normally for STEM $I_s > I_0$ so that I_e will flow from ground to the

specimen as shown in Fig. 5a. Thus if the specimen is not grounded then it will charge positively.

When a specimen consisting of a *p-i-n* junction (Fig. 5b) is irradiated by light, electron-hole pairs form and electron currents, I_{neh} and I_{peh} , flow from the *n* contact to the *p* contact, respectively. For such a junction, $I_{neh} = I_{peh} = I_{pn}$, where I_{pn} is the *p-i-n* junction current, and can be measured directly using a differential amplifier whose inputs are

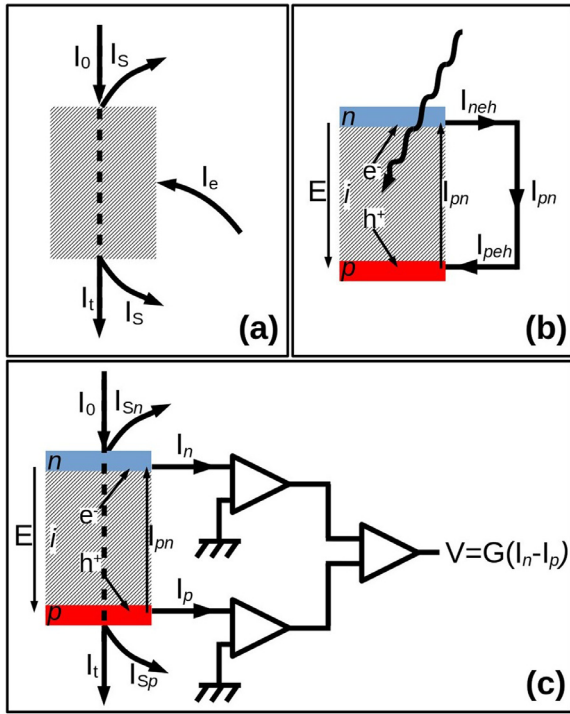


Fig. 5. (a) Diagram showing the currents generated in a thin TEM specimen when irradiated by a high-energy electron beam and electrically connected to ground. (b) Current generated in a *p-i-n* junction when irradiated by neutral particles such as photons. (c) Currents generated in a plan-view *p-i-n* junction in a TEM when irradiated by high energy electrons. Also shown is a diagram of the differential amplifier used in our experiments to measure the EBIC current. The currents are defined as follows: I_0 , incident beam current; I_t , transmitted beam current (including diffracted and inelastically scattered electrons); I_s , secondary, backscattered and Auger electron current, I_{sn} and I_{sp} , secondary, backscattered and Auger electron currents emitted from the *n* and *p* sides, I_e , ground current from the specimen; I_{neh} and I_{peh} electron current generated due to the creation of electron-hole pairs from an incident particle (photon in (b) or electron in (c)) from the *n* contact to the *p* contact; I_n and I_p , currents from the *n* and *p* contacts as defined in Eqs. (4) and (5). Note that the arrows show the assumed flow of electrons (not the conventional current).

connected to the *n* and *p* contacts.

In our STEM experiment we have a combination of the above two cases where our plan-view *p-i-n* junction is scanned by an electron beam passing through both the *p* and *n* parts of the junction simultaneously as shown in Fig. 5c. We would like to measure the electron-hole pair current, I_{pn} , as in Fig. 5b and hence we connected our differential amplifier to the *n* and *p* contacts leaving the specimen otherwise electrically isolated. Unfortunately I_{pn} , I_n and I_p are now all different to each other as there are additional currents flowing to and from the *n* and *p* contacts compared to the case shown in Fig. 5b. To understand the origin of the current measured by the differential amplifier we also have to take into account the various currents due to the electron beam as shown in Fig. 5a.

We consider the currents flowing to and from the *n* and *p* contacts separately. For the equations we take the direction of the electron currents to be as shown in Fig. 5c. For the convenience of considering the currents in the amplifier, the currents I_n and I_p are both assumed to flow out from the contacts towards the amplifier (note that the direction of I_p is opposite to I_{peh} in Fig. 5b which flows towards the *p* contact). As we will see later the actual direction of electron flow and thus whether I_n and I_p are positive or negative depends on the magnitude of the other currents flowing from the contacts.

The currents entering the *n* contact must be equal to the currents exiting the *n* contact and are given by (see Fig. 5c, where the arrows

show the directions the electron currents are assumed to flow)

$$f_n(I_0 - I_t) + I_{pn} = I_n + I_{sn}$$

Thus the current flowing from the *n* contact to the amplifier is

$$I_n = f_n I_{abs} - I_{sn} + I_{pn} \quad (4)$$

where f_n is the fraction of the absorbed incident beam current, I_{abs} , that flows through the *n* contact. We have also separated the secondary electron current, I_s , into the components emitted from the *n* contact, I_{sn} , and the *p* contact, I_{sp} . In doing so we have assumed that all the secondary electrons emitted from the *n* contact give rise to a current flowing only from the *n* contact and similarly for the *p* contact.

Likewise the currents entering and exiting the *p* contact will be given by

$$(1 - f_n)(I_0 - I_t) = I_p + I_{sp} + I_{pn}$$

Thus the current flowing from the *p* contact to the amplifier is

$$I_p = (1 - f_n)I_{abs} - I_{sp} - I_{pn} \quad (5)$$

It can be seen from Eqs. (4) and (5) that the sign (and thus the direction) of I_n and I_p depend on the relative magnitudes of the other currents at the contacts. So for example I_n will flow away from the *n* contact towards the amplifier (in the direction of the arrow in Fig. 5c) if I_{pn} is large and will flow towards the *n* contact if I_{sn} is large.

The total current flowing from the ground, I_e (see Fig. 5a), is just the sum of the currents from the *n* and *p* contacts (negative because I_e is the current towards the specimen while I_n and I_p are defined as flowing away from the specimen)

$$I_e = -(I_n + I_p) = (I_{sn} + I_{sp}) - I_{abs} \quad (6)$$

The current measured by the differential amplifier and thus the “EBIC” signal shown in Fig. 2a and *i* is the difference between the ground currents flowing to the *n* and the *p* contacts

$$I_{EBIC} = I_n - I_p = (2f_n - 1)I_{abs} + (I_{sp} - I_{sn}) + 2I_{pn} \quad (7)$$

The different current components in Eq. (7) are shown schematically in Fig. 5c.

The EBIC signal, I_{EBIC} , thus has three components. The last component of this signal, $2I_{pn}$, is the electron beam induced current we would like to measure. Given that the energy required to create electron-hole pairs is of the order of a few eV, a 200 kV incident electron could create up to 10^5 electron-hole pairs. In practice, fewer will be generated as only a small fraction of the incident energy is lost in the region in the *p-i-n* junction but we would still expect I_{pn} to be the strongest signal.

The component $(2f_n - 1)I_{abs}$, depends on both the incident beam current absorbed in the specimen and the fraction of this current flowing from each contact. The absorbed current, I_{abs} , will resemble the ADF signal since the heavier elements that give rise to higher ADF signals also reduce the transmitted beam current, I_t . For thin specimens I_{abs} will be small compared to I_0 and also smaller than the secondary electron currents I_{sn} and I_{sp} . Also, if the *n* and *p* regions are of similar thickness and density then the fraction absorbed in the *n* contact, f_n , will be close to 0.5, making $(2f_n - 1)$ close to zero and further reducing the effect of this component on the EBIC signal.

$(I_{sp} - I_{sn})$ is the difference between the secondary electron signals from the *p* and *n* contacts. We should thus see a superposition of the secondary electron signals from the top and bottom of the specimen but with opposite signs. The bottom surface, on the *p* contact side, is the flat SiN_x membrane, so it should not induce any significant spatial modulation on I_{sp} in this experiment and I_{sp} should therefore contribute only a constant offset to the EBIC image. Secondary electrons have energies of around 5 to 50 eV and thus fewer should be generated per 200 kV incident electron than for electron-hole pairs.

We are now able to understand the contrast seen in our EBIC images shown in Fig. 2a and *i*. The most obvious feature, the dark circle covering most of Fig. 2i resembles the feature in the secondary electron

images in Fig. 4a–c. As these images were taken looking at the top surface, i.e. the n contact of the cell, this feature must be due to I_{sn} , the secondary electron current from the n contact. The darker contrast in Fig. 2i indicates a reduction in the SE current collected on the n side at these positions. Our explanation is that the SE electrons generated from the Al and to a lesser extent from the perovskite layer are absorbed by this nitrogen-rich area located on the top surface of the Al layer (and the nitrogen-rich area itself produces few secondary electrons), resulting in a lower I_{sn} current at these locations.

We also see a fainter component of Fig. 2i that resembles the HAADF or ADF images in Fig. 2b and c. This component must come from the absorbed current I_{abs} which will be greatest for the heavy elements present in the perovskite layer. The contrast is similar to but not the same as that in Fig. 2b and c suggesting that f_n in $(2f_n - 1)I_{abs}$ is close to 0.5. This makes the contribution of I_{abs} to I_{EBIC} vary depending on how close each feature is to the n or p contacts.

We do not see any contrast in the EBIC image in Fig. 2i that can be associated with secondary electron emission from the bottom surface. This is expected as the bottom surface is a uniform layer of silicon nitride support film. We also do not see any contrast that could be interpreted as coming from the EBIC signal, I_{pn} in Fig. 2i. While this could be because the EBIC signal is too weak compared to the secondary electron and absorption signals, it also suggests that any EBIC signal present must be relatively uniform across the area of the junction imaged. We were expecting any defects present in the cell such as pinholes or short circuits to show up as areas of reduced EBIC and the absence of any such areas suggests that our cell is uniform.

6. Conclusions

We have presented an innovative approach to prepare a sample for *in situ* TEM biasing experiments without introducing artefacts during sample preparation. Moreover, the active and air-sensitive part of our device is encapsulated in between the two electrical contacts, which prevents degradation and insures low contact resistance to the solar cell. We have also shown that the EBIC signal can be easily recorded using available image acquisition hardware by using a home-made amplifier.

An analysis of the currents contributing to the signal measured by our differential amplifier shows that it is impossible to separate the effects of absorption of the primary beam, secondary electron emission and the electron beam-induced current in the cell. This is a general conclusion that applies to all EBIC measurements in electron microscopes. The resulting image thus depends mainly on the largest of these components. We can reduce the absorbed current signal by minimising the thickness of the specimen and minimising the atomic number of the elements present (or at least the variation of the atomic number across the specimen). The secondary electron current can be reduced by ensuring that both surfaces are as uniform as possible. Coating both surfaces with a thin layer of a low atomic number element such as carbon may also help in reducing the secondary electron signal. Ultimately, though, the EBIC signal, I_{pn} , will only dominate if it is significantly greater than the other signals.

Contributions

All authors have participated in (a) conception and design, or analysis and interpretation of the data; (b) drafting the article or revising it critically for important intellectual content; and (c) approval of the final version.

Declaration of Competing Interest

None.

Acknowledgements

We are grateful to Thomas Duden for the fabrication and operation of the amplifier during the EBIC experiments. M.D. acknowledges financial support from Nanyang Technological University start-up grant M4081924.

Supplementary materials

Supplementary material associated with this article can be found, in the online version, at [doi:10.1016/j.ultramic.2020.113047](https://doi.org/10.1016/j.ultramic.2020.113047).

References

- [1] H.J. Leamy, Charge collection scanning electron microscopy, *J. Appl. Phys.* 53 (1982) R51–R80, <https://doi.org/10.1063/1.331667>.
- [2] H. Blumtritt, R. Gleichmann, J. Heydenreich, H. Johansen, Combined scanning (EBIC) and transmission electron microscopic investigations of dislocations in semiconductors, *Phys. Status Solidi A* 55 (1979) 611–620, <https://doi.org/10.1002/psa.2210550231>.
- [3] A. Ourmazd, A theoretical interpretation of the electrical behaviour of individual edge dislocations in Si as determined by combined EBIC/TEM studies, *Krist. Tech.* 16 (1981) 137–146, <https://doi.org/10.1002/crat.19810160204>.
- [4] M. Mazzer, E. Grünbaum, K.W.J. Barnham, J. Barnes, P.R. Griffin, D.B. Holt, J.L. Hutchison, A.G. Norman, J.P.R. David, J.S. Roberts, R. Grey, Study of misfit dislocations by EBIC, CL and HRTEM in GaAs/InGaAs lattice-strained multi-quantum well p-i-n solar cells, *Mater. Sci. Eng. B* 42 (1996) 43–51, [https://doi.org/10.1016/S0921-5107\(96\)01681-9](https://doi.org/10.1016/S0921-5107(96)01681-9).
- [5] D. Fathy, T.G. Sparrow, U. Valdrè, Observation of dislocations and microplasma sites in semiconductors by direct correlations of STEBIC, STEM and ELS, *J. Microsc.* 118 (1980) 263–273, <https://doi.org/10.1111/j.1365-2818.1980.tb00273.x>.
- [6] T.G. Sparrow, U. Valdrè, Application of scanning transmission electron microscopy to semiconductor devices, *Philos. Mag.* 36 (1977) 1517–1528, <https://doi.org/10.1080/14786437708238532>.
- [7] P.D. Brown, C.J. Humphreys, Scanning transmission electron beam induced conductivity investigation of a Si/Si_{1-x}Ge_x/Si heterostructure, *J. Appl. Phys.* 80 (1996) 2527–2529, <https://doi.org/10.1063/1.363038>.
- [8] W.A. Hubbard, M. Mecklenburg, H.L. Chan, B.C. Regan, Secondary electron contrast in STEM Electron Beam-Induced Current (EBIC): a path towards mapping electronic structure, *Microsc. Microanal.* 24 (2018) 1846–1847, <https://doi.org/10.1017/S1431927618009716>.
- [9] E.R. White, A. Kerelsky, W.A. Hubbard, R. Dhall, S.B. Cronin, M. Mecklenburg, B.C. Regan, Imaging interfacial electrical transport in graphene–MoS₂ heterostructures with electron-beam-induced-currents, *Appl. Phys. Lett.* 107 (2015) 223104, <https://doi.org/10.1063/1.4936763>.
- [10] E. Edri, S. Kirmayer, S. Mukhopadhyay, K. Gartsman, G. Hodes, D. Cahen, Elucidating the charge carrier separation and working mechanism of CH₃NH₃PbI_{3-x}Cl_x perovskite solar cells, *Nat. Commun.* 5 (2014), <https://doi.org/10.1038/ncomms4461>.
- [11] Q. Jeangros, M. Duchamp, J. Werner, M. Kruth, R.E. Dunin-Borkowski, B. Niesen, C. Ballif, A. Hessler-Wyser, *In situ* TEM analysis of organic-inorganic metal-halide perovskite solar cells under electrical bias, *Nano Lett.* (2016), <https://doi.org/10.1021/acs.nanolett.6b03158>.
- [12] E. Miyazaki, K. Miyaji, Enhancement of reverse current in semiconductor diodes by electron bombardment, *Jpn. J. Appl. Phys.* 2 (1963) 129–130, <https://doi.org/10.1143/JJAP.2.129>.
- [13] V.K.S. Ong, J.C.H. Phang, D.S.H. Chan, A direct and accurate method for the extraction of diffusion length and surface recombination velocity from an EBIC line scan, *Solid-State Electron* 37 (1994) 1–7, [https://doi.org/10.1016/0038-1101\(94\)90096-5](https://doi.org/10.1016/0038-1101(94)90096-5).
- [14] C. Donolato, Theory of beam induced current characterization of grain boundaries in polycrystalline solar cells, *J. Appl. Phys.* 54 (1983) 1314–1322, <https://doi.org/10.1063/1.332205>.
- [15] C. Donolato, On the analysis of diffusion length measurements by SEM, *Solid-State Electron* 25 (1982) 1077–1081, [https://doi.org/10.1016/0038-1101\(82\)90144-7](https://doi.org/10.1016/0038-1101(82)90144-7).
- [16] K.L. Luke, O. Von Roos, An EBIC equation for solar cells, *Solid-State Electron* 26 (1983) 901–906, [https://doi.org/10.1016/0038-1101\(83\)90062-X](https://doi.org/10.1016/0038-1101(83)90062-X).
- [17] C. Donolato, Charge collection in a Schottky diode as a mixed boundary-value problem, *Solid-State Electron* 28 (1985) 1143–1151, [https://doi.org/10.1016/0038-1101\(85\)90195-9](https://doi.org/10.1016/0038-1101(85)90195-9).
- [18] J.-M. Bonard, J.-D. Ganière, Quantitative analysis of electron-beam-induced current profiles across p-n junctions in GaAs/Al_{0.4}Ga_{0.6}As heterostructures, *J. Appl. Phys.* 79 (1996) 6987–6994, <https://doi.org/10.1063/1.361464>.
- [19] C.M. Parish, P.E. Russell, On the use of Monte Carlo modeling in the mathematical analysis of scanning electron microscopy-electron beam induced current data, *Appl. Phys. Lett.* 89 (2006) 192108, <https://doi.org/10.1063/1.2385212>.
- [20] C. Donolato, An analytical model of SEM and STEM charge collection images of dislocations in thin semiconductor layers. II. EBIC images of dislocations, *Phys. Status Solidi A* 66 (1981) 445–454, <https://doi.org/10.1002/psa.2210660205>.
- [21] M. Duchamp, V. Migunov, A.H. Tavabi, A. Mehonc, M. Buckwell, M. Munde, A.J. Kenyon, R.E. Dunin-Borkowski, *In situ* transmission electron microscopy of

- resistive switching in thin film silicon oxide layers, *Resolut. Discov.* 1 (2016) 27–33, <https://doi.org/10.1556/2051.2016.00036>.
- [22] S. Sun, T. Salim, N. Mathews, M. Duchamp, C. Boothroyd, G. Xing, T.C. Sum, Y.M. Lam, The origin of high efficiency in low-temperature solution-processable bilayer organometal halide hybrid solar cells, *Energy Environ. Sci.* 7 (2013) 399–407, <https://doi.org/10.1039/C3EE43161D>.
- [23] A. Kovács, R. Schierholz, K. Tillmann, FEI Titan G2 80-200 CREWLEY, J. Large-Scale Res. Facil. JLSRF. 2 (2016) 43, <https://doi.org/10.17815/jlsrf-2-68>.
- [24] H. Seiler, Secondary electron emission in the scanning electron microscope, *J. Appl. Phys.* 54 (1983) R1–R18, <https://doi.org/10.1063/1.332840>.
- [25] W. Chesarek, K. Mitchell, A. Mason, L. Fabick, EBIC analysis of CuInSe₂ devices, *Sol. Cells* 24 (1988) 263–270, [https://doi.org/10.1016/0379-6787\(88\)90077-4](https://doi.org/10.1016/0379-6787(88)90077-4).
- [26] H. Inada, D. Su, R.F. Egerton, M. Konno, L. Wu, J. Ciston, J. Wall, Y. Zhu, Atomic imaging using secondary electrons in a scanning transmission electron microscope: experimental observations and possible mechanisms, *Ultramicroscopy* 111 (2011) 865–876, <https://doi.org/10.1016/j.ultramic.2010.10.002>.